



Title	Adaptation of Patterns of Motile Filaments under Dynamic Boundary Conditions
Author(s)	Inoue, Daisuke; Gutmann, Greg; Nitta, Takahiro; Kabir, Arif Md. Rashedul; Konagaya, Akihiko; Tokuraku, Kiyotaka; Sada, Kazuki; Hess, Henry; Kakugo, Akira
Citation	ACS nano, 13(11), 12452-12460 <a href="https://doi.org/10.1021/acsnano.9b01450">https://doi.org/10.1021/acsnano.9b01450</a>
Issue Date	2019-11
Doc URL	<a href="http://hdl.handle.net/2115/79404">http://hdl.handle.net/2115/79404</a>
Rights	This document is the Accepted Manuscript version of a Published Work that appeared in final form in ACS nano, © American Chemical Society after peer review and technical editing by the publisher. To access the final edited and published work see <a href="https://pubs.acs.org/doi/10.1021/acsnano.9b01450">https://pubs.acs.org/doi/10.1021/acsnano.9b01450</a> .
Type	article (author version)
Additional Information	There are other files related to this item in HUSCAP. Check the above URL.
File Information	Revised main ManuscriptRV2.pdf



[Instructions for use](#)

# **Adaptation of Patterns of Motile Filaments under Dynamic Boundary Conditions**

*Daisuke Inoue<sup>1</sup>, Greg Gutmann<sup>2</sup>, Takahiro Nitta<sup>3</sup>, Arif Md. Rashedul Kabir<sup>1</sup>, Akihiko Konagaya<sup>2</sup>,  
Kiyotaka Tokuraku<sup>4</sup>, Kazuki Sada<sup>1,5</sup>, Henry Hess<sup>6</sup> and Akira Kakugo<sup>1,5</sup>†*

<sup>1</sup>Faculty of Science, Hokkaido University, Sapporo 060-0810, Japan

<sup>2</sup>Department of Computer Science, Tokyo Institute of Technology, Yokohama, 226-8502, Japan

<sup>3</sup> Applied Physics Course, Faculty of Engineering, Gifu University, Gifu 501-1193, Japan.

<sup>4</sup>Department of Applied Sciences, Muroran Institute of Technology, Muroran 050-8585, Japan

<sup>5</sup> Graduate School of Chemical Sciences and Engineering, Hokkaido University, Sapporo 060-0810,  
Japan

<sup>6</sup> Department of Biomedical Engineering, Columbia University, New York, NY 10027, USA

† Corresponding author. E-mail: kakugo@sci.hokudai.ac.jp

Telephone/fax: +81-11-706-3474

## **ABSTRACT**

Boundary conditions are important for pattern formation in active matter. However, it is still not well-understood how alterations in the boundary conditions (dynamic boundary conditions) impact pattern formation. To elucidate the effect of dynamic boundary conditions on the pattern formation by active matter we investigate an *in vitro* gliding assay of microtubules on a deformable soft substrate. The dynamic boundary conditions were realized by applying mechanical stress through stretching and compression of the substrate during the gliding assay. A single cycle of stretch-and-compression (relaxation) of the substrate induces perpendicular alignment of microtubules relative to the stretch axis, whereas repeated cycles resulted in zigzag patterns of microtubules. Our model shows that the orientation angles of microtubules correspond to the direction to attain smooth movement without buckling, which is further amplified by the collective migration of the microtubules. Our results provide an insight to understand the rich dynamics in self-organization arising in active matter subjected to time-dependent boundary conditions.

## **KEYWORDS**

active matter; adaptation; collective motion; microtubules; mechanical stimuli; motor protein; self-organization

Different types of active matter are well known for their fascinating pattern formation in crowded conditions.<sup>1-5</sup> Theoretical<sup>1, 6-8</sup> and experimental studies<sup>9-21</sup> suggest that the pattern formation is dependent on the local interactions among the individual units. Boundary conditions, *e.g.* geometric confinement,<sup>10, 12, 13, 19, 25</sup> and the environment,<sup>26-29</sup> also play a critical role in the organization of active matter. In particular, inducing asymmetry in the environment by a magnetic field,<sup>11, 26, 27</sup> mechanical field,<sup>29</sup> flow field,<sup>25</sup> or light<sup>9</sup> can affect the pattern formation of active matters. However, self-organization of active matter under dynamic boundary conditions has been receiving growing interest,<sup>30-35</sup> in which new phenomena may emerge from the interacting dynamics of active matter and the time-dependence of the boundary conditions. Cytoskeletal filaments driven by motor proteins on a substrate are now a classic realization of active matter.<sup>13-25, 30</sup> A deformable substrate would provide a means to modulate the boundary conditions for the gliding cytoskeletal filaments. Recently, we developed a system that allows the application of uniaxial stretching stimuli to microtubules driven by kinesin-1 on an elastomer substrate (Figure 1a, Figure S1).<sup>36</sup> Our system allows the application of various modes of stretching to the gliding cytoskeletal filaments, which in turn facilitates manipulation of the dynamic boundary conditions. Here, by deforming the substrate through stretching and compression, we investigate the effect of dynamic boundary conditions on the pattern formation by gliding microtubules in crowded conditions.

## RESULTS AND DISCUSSION

**Application of single-step stretching:** We first initiated the formation of a streaming flow of microtubules on a kinesin coated silicone elastomer substrate by absorbing microtubules at a surface density ( $\rho$ ) above the previously determined threshold of  $\rho = 6 \times 10^5$  filaments per  $\text{mm}^2$  (Figures 1a-c and Figure S1, Movie S1).<sup>20, 36</sup> The streaming flow was fully formed two hours after the initiation of microtubule gliding. Then we applied a single stretching cycle where we elongated the substrate to a strain of 75% at a strain rate of  $\dot{\epsilon} = 0.012 \text{ s}^{-1}$ , and compressed it back to its original length at the

same rate (Figure 1d). After the stretching cycle, the wavy streaming pattern of the gliding microtubules was destabilized, and the streaming flow reorganized itself into a flow aligned perpendicular to the stretching axis (Figures 1e and 1f, Movie S2). The perpendicular alignment of the flow relative to the stretch axis developed over a timescale of a few minutes after the stretching cycle. After reaching a steady state the alignment remained stable for several hours when the microtubule density was higher than the critical density required to form the streaming flow. This is quantified by the time dependence of the nematic order parameter,  $S$ , obtained by analysing the time-lapse fluorescence microscopy images (Figure 1g).<sup>20</sup> For microtubule densities lower than the critical density, the perpendicular alignment decayed to a random state within minutes as we reported in our previous work<sup>36</sup> (Figure 1g and Figure S3). To monitor the movement of microtubules in the highly dense streaming flow, we used Alexa488 (green) labelled microtubules mixed with TAMRA (red) labelled microtubules and observed the formation of the streaming flow. By monitoring the green microtubules we found that microtubules that deviated from a path aligned with the stream were soon entrained by collisions with nearby microtubules (Figure 2a, Movie S3, S4). Thus, the long-lived stability originates from the nematic interaction between the neighbouring microtubules.<sup>18</sup> The nematic interaction may also catalyse the orientation process of microtubules forming streaming flow since the stretch induced orientation of microtubules was amplified with time, whereas it decayed after stopping the stretching in the absence of the nematic interaction (Figure 1g, 2b Figure S2, S3). However, even in the presence of the nematic interaction, the reorganization did not take place when the applied strain was smaller than 20% regardless of the strain rate in the range of 0.012 to 0.2 s<sup>-1</sup> (Figure S4). This result suggests that there is a critical strain,  $\epsilon_c$  to amplify the orientation of microtubules by the nematic interaction. As reported in our previous work, the application of higher strain increased the number of perpendicularly oriented microtubules against the stretch axis just after stopping the compression process of the substrate (Figure S5).<sup>36</sup> The amplification of the global orientation might have been driven by the small number of entities which were oriented by stretching

(Figure 2b, c). This hypothesis is supported by a Vicsek model-based simulation which is provided in the Supplementary Information (Figure S6, S7, Movie S5).

To check that realignment was caused by the substrate deformation and not by the fluid shear flow caused by the substrate deformation, the substrate was replaced by a glass substrate in the gliding assay of microtubules. The movable frame of the stretch chamber was moved back and forth at a speed equal to that used to stretch substrate at the strain of 75% and a strain rate of  $\dot{\epsilon} = 0.012 \text{ s}^{-1}$ . However, no changes in orientation were observed for the gliding microtubules, which confirms that the realignment of microtubules on the elastomer substrate is not resulting from fluid shear flow generated by the stretching/compression of the elastomer substrate (Figure S8).

**Application of cyclic stretching:** Cyclic stretching (repeated cycles of ‘elongation of the elastomer substrate followed by compression back to the initial length’) stimulated a different response of the microtubules compared to that observed in a single stretching cycle. Cyclic stretching with a strain of 20% at a strain rate of  $0.04 \text{ s}^{-1}$  and a frequency of 0.1 Hz reorganized the streaming flow of microtubules into a unique zigzag pattern with two characteristic orientation angles of  $64.7 \pm 2.8^\circ$  and  $116.4 \pm 1.1^\circ$  (mean  $\pm$  s.d., Figure 3a and Figure S9). Since pattern formation was not observed in the single stretching cycle experiment at a strain of 20%, the zigzag pattern formation under cyclic stretching must originate from the accumulation of small changes in microtubule alignment which are not detectable in the single stretching cycle experiments. The formation of the zigzag patterns was not affected by changes in the stretching frequency within the range of 0.1 Hz to 1 Hz (Figures 3b to 3d and Figure S9, Movie S6). The distance between two consecutive bending points of the zigzag track (half a wavelength) was broadly distributed ( $113 \pm 57 \text{ }\mu\text{m}$  and  $99 \pm 67 \text{ }\mu\text{m}$  (mean  $\pm$  s.d.) for high density and low-density areas of microtubules, respectively;  $n = 50$ , Figure S10). A comparison of the same field of view between before and after cyclic stretching shows that the initial distribution of microtubules appears to determine the wavelength of the zigzag tracks (Figure S11).

Since the microtubule streams are wavy on the length scale of the microtubule trajectory persistence length (measured to be  $386 \pm 81 \mu\text{m}$ ), the distance between bending points is of similar magnitude. The zigzag pattern of the microtubules exhibited prolonged stability and retained their orientation angles (Figure S12, Movie S7). This indicates that the nematic interaction between microtubules also plays an important role in maintaining the zigzag pattern as observed in the long-lived perpendicular orientation of microtubules in the single-step stretching experiments. *In vitro* experiments below the critical density of microtubules showed that the alignment with the characteristic angles was not as prominent as observed in the high microtubule density conditions although small peaks were observed around the two characteristic orientation angles in the angular distribution of microtubules (Figure S13). Such weak response of microtubules to mechanical stimuli was also observed in the single stretching cycle experiment (Figure 1g, Figures S4), which suggests that streaming reinforces the realignment process of microtubules (detailed discussion is available in the Supplementary Information).

Since it is conceivable that the stretching/compression cycles do not only affect the microtubule organization but also the distribution of kinesin on the surface, we imaged the GFP-kinesin after the formation of the zigzag patterns and found that the uniform distribution of kinesin motors was maintained (Figure S14). We attribute this to the strong bonds between the surface, the anti-GFP antibody, and the GFP-kinesin, which make it more likely that unbinding and rebinding between kinesin-microtubule occurs during the deformation of the elastomer substrate.

**Mechanism of orientation of microtubules:** The orientation of gliding microtubules is determined by the leading tip, because the middle and tail of the microtubule follow the tip along the kinesin attachment points to the surface.<sup>37</sup> On a smooth and static kinesin-coated surface, the movement of an individual microtubule is a persistent random walk with a trajectory persistence length of  $386 \pm 81 \mu\text{m}$ , because the large stiffness of the microtubule permits only small thermal fluctuations of the

tip direction as the microtubule advances.<sup>38</sup> This behaviour can be reproduced in Brownian Dynamics simulations,<sup>39</sup> which include the force-induced detachment of kinesin motors from the microtubule.<sup>40</sup> As our previous study has shown experimentally and in Brownian Dynamics simulations,<sup>36</sup> a gliding microtubule aligned with the stretch axis will remain straight and aligned during the stretching phase (although the motors will detach and reattach to accommodate the substrate strain), while it will buckle during the compression phase. The tip of the buckled microtubule will now be oriented under an angle to the stretch axis, and the microtubule will glide in a new direction. Microtubules aligned perpendicularly to the stretch axis will experience the same process in reverse, because the strain in the perpendicular direction is reversed in sign but smaller (depending on the Poisson ratio) (Figure 4a, Figure S15). Buckling followed by stretching will largely maintain the orientation of the tip according to the stretch axis, so that overall a perpendicular orientation is preferred. This preferable orientation is amplified and stabilized for a long time due to another factor, nematic interactions between microtubules (Figure 1g, Figure S7).

The emergence of zigzag patterns in cyclic stretching is surprising in the context of the above explanation, because an additional factor has not been described: During uniaxial stretching and compression, there are two directions along which the substrate neither expands nor contracts because the extension/compression along the stretch axis is precisely balanced by the compression/extension of the substrate perpendicular to the stretch axis (Figure 4b). These angles can be geometrically calculated to correspond to  $\arctan(1/\nu)$ , where  $\nu$  is the Poisson ratio. For  $\nu = 0.43$  at 20% strain, this corresponds to angles of  $66.7^\circ$  and  $113.3^\circ$  which matches the experimentally observed angles of the zigzag pattern (Figure 4c). Our Brownian dynamics simulations support this as well: At this relatively high Poisson ratio, microtubules aligned at angles other than the characteristic ones buckled (Figure S16). In contrast, a microtubule aligned at  $66^\circ$  against the stretch axis did not show such buckling (Figure S16). The preference for these deformation-free angles combined with the stabilizing nematic interactions explains the observation of zigzag patterns at low strain.

Interestingly, the disappearance of the zigzag pattern at higher strains ( $\geq 40\%$ ) likely originates from the strain-dependent Poisson ratio of the substrate material. At 40% strain, the Poisson ratio has dropped to 0.3 (Figure S15) with deformation-free angles of  $73^\circ$  and  $107^\circ$ . Yet, the system compromises on a  $90^\circ$  alignment instead of a zigzag orientation (Figure S17). This abrupt transition merits further study in the future. Thus the zigzag pattern is present only in a narrow window, where the strain is large enough to destabilize angles other than the deformation-free angles and small enough so that the Poisson ratio is high and the system does not settle on perpendicular alignment.

**Application of radial stretching:** Based on the above discussed mechanism of the pattern formation, we are able to design patterns. By indenting the elastomer substrate from the bottom with a spherical-shaped indenter tip (diameter: 1 mm) by 10 mm at a rate of  $0.08 \text{ mm s}^{-1}$ , we applied radial stretching and returned the substrate to the undeformed state. A 3D view of the indented substrate and strain distribution are shown in Figure S18. As explained above, when the elastomer substrate is subjected to stretching at a high stretching strain, microtubules orient perpendicularly against the axis of the maximum principal stress. Judging from the shape and stress pattern of the indented substrate (Figure S18), the maximum principal stress axes should be radially distributed around the indenter tip as shown in the schematic diagram in Figure 5d but not toward azimuthal axes.<sup>41, 42</sup> The perpendicular orientation against these radial stress axes during indentation resulted in the formation of vortex alignment of microtubules around the indenter tip (Figure 5a-e and Figure S19, Movie S8). However, at the periphery of the substrate, vortex formation was not prominently observed even after 30 min of indentation (Figure 5f, and Figure S19) since the local strain was below the critical strain  $\varepsilon_c$  (Figure S2b and S18). However, these non-oriented microtubules were finally incorporated into the large vortex, which resulted in the growth of the vortex with time (Figures 5f and 5g). The diameter of the vortex eventually reached 15 mm after 24 hours, which is 10 million times larger than the length of the individual microtubules. The growth of the vortex is again due to the nematic interaction between

microtubules which forces non-oriented microtubules to align along the orientated microtubules. The circular trajectories of the microtubules were sustained even after a part of the vortex was scratched, due to quick repair of the pattern by the neighbouring motile microtubules (Figures 5i and 5h).

## CONCLUSIONS

In conclusion, by applying mechanical stimuli to microtubules gliding on a deformable substrate, we investigated the effect of time-dependent boundary conditions on the pattern formation of active matter *i.e.*, kinesin-driven microtubules. We found that the existence of orientation angles, which do not experience stretching or compression due to the Poisson ratio of the silicone elastomer substrate at 20% strain ( $\nu = 0.43$ ), creates dynamically stable gliding directions for the microtubules. All other gliding directions are unstable, and the microtubule orientations slowly converge towards either one of the stable angles, which makes repeated stretching and compression cycles necessary for the zigzag pattern formation. At high strains ( $\geq 40\%$ ) the Poisson ratio of the silicone elastomer substrate is smaller ( $\nu \leq 0.3$ ), which increases the deformation free angles and leads the system to settle on perpendicular alignment. The nematic interactions between microtubules at high densities are critical for sharpening and stabilizing the process. The programmable reorganization of our rod-like motile agents into different patterns reflecting the mode of stretching demonstrates the flexibility and adaptability of the active system to its dynamic environment. These findings highlight the rich dynamics in self-organization of active matter arising from the time-dependent boundary conditions.

## MATERIALS AND METHODS

**Expression and purification of proteins:** Tubulin was purified from porcine brain using a high-concentration PIPES buffer (1 M PIPES, 20 mM EGTA, 10 mM MgCl<sub>2</sub>; pH adjusted to 6.8 using KOH). High-molarity PIPES buffer and BRB80 buffer were prepared using PIPES from Sigma.<sup>43</sup> Recombinant GFP-fused kinesin-1 consisting of the first 560 amino acid residues of human kinesin-1 (K560-GFP-His6) was prepared by partially modifying previously reported expression and purification methods.<sup>44</sup> In brief, after elution of kinesin from the Ni-NTA column in the original protocol, dialysis was performed to reduce the salt concentration in the kinesin elution buffer by using a dialysis tube (50 kD, 7.5 mm diameter; model Spectra/Por 6, Spectrum, Houston, TX). Then the kinesin was subjected to an additional microtubule affinity purification step as described in the original literature. The MAP4 fragment, which was used as isoform fragment polypeptides (PA4T) containing the microtubule-binding domain, was purified as described in literature.<sup>45</sup>

**Preparation of labelled tubulin and microtubules:** Rhodamine- and Alexa488-labelled tubulin were prepared using 5/6-carboxy-tetramethyl-rhodamine succinimidyl ester (TAMRA-SE; Invitrogen) and Alexa488 succinimidyl ester (Invitrogen), respectively, according to a standard technique.<sup>46</sup> The labelling ratio was 1.0 for both cases, and was estimated by measuring the absorbance of the protein at 280 nm and that of TAMRA and Alexa488 at 555 nm and 488 nm with a UV spectrophotometer (Nanodrop 2000c). Rhodamine- or Alexa488-labelled microtubules were obtained by polymerising a mixture of rhodamine- or Alexa488-labelled tubulin (TT or AT) and non-labelled tubulin (WT) (AT or TT: WT = 4:1; final tubulin concentration, 55.6 μM) using guanosine triphosphate (GTP) at 37 °C. The microtubule solution was then diluted with motility buffer (80 mM PIPES, 1 mM EGTA, 2 mM MgCl<sub>2</sub>, 0.5 mg mL<sup>-1</sup> casein, 1 mM DTT, 10 μM paclitaxel and ~1% DMSO; pH 6.8).

***In vitro* gliding assay:** A polydimethylsiloxane-based polymer substrate ( $6.8 \times 5 \times 0.05 \text{ mm}^3$ ,  $L \times W \times T$ ; Fuso Rubber Industry Co., Ltd) was fixed to the movable frame of the stretch chamber. The surface of elastomer substrate was exposed to plasma for 1 min by a plasma etcher (SEDE-GE; Meiwafoysis Co., Ltd.) to obtain a hydrophilic surface. Anti-GFP antibody (Invitrogen) at  $0.04 \text{ mg mL}^{-1}$  ( $10 \text{ }\mu\text{L}$ ) was applied to the surface of the substrate (Figure S1d). After incubation for 3 min, the surface of the substrate was washed with  $5 \text{ }\mu\text{L}$  of casein solution ( $80 \text{ mM PIPES}$ ,  $1 \text{ mM EGTA}$ ,  $1 \text{ mM MgCl}_2$ ,  $\sim 2 \text{ mg mL}^{-1}$  casein; pH adjusted to 6.8 using KOH) and incubated for 2 min. Then,  $10 \text{ }\mu\text{L}$  of  $200 \text{ nM}$  kinesin solution in motility buffer was introduced and incubated for 3 min to bind the kinesin to the antibody at a density of approximately  $400 \text{ molecules }\mu\text{m}^{-2}$ . The surface of the elastomer substrate was washed with  $10 \text{ }\mu\text{L}$  of motility buffer. Next,  $10 \text{ }\mu\text{L}$  of  $5 \text{ }\mu\text{M}$  microtubule solution was introduced and incubated for 3 min, followed by washing with  $20 \text{ }\mu\text{L}$  of motility buffer;  $5 \text{ }\mu\text{L}$  of  $0.25 \text{ }\mu\text{M}$  isoform fragment polypeptide of MAP4 (MAP4 fragment; PA4T) containing a microtubule-binding domain which induces weak attractive interaction among microtubule filaments to maintain the density of microtubules for a long time<sup>20</sup> and incubated for 3 min, followed by washing with  $20 \text{ }\mu\text{L}$  of motility buffer. Then,  $100 \text{ }\mu\text{L}$  of motility buffer supplemented with  $10 \text{ mM ATP}$  and  $0.33 \text{ wt\%}$  methylcellulose (ATP buffer), which induces attractive interactions among microtubules due to the depletion force, was dropped on the cover glass ( $40 \times 50 \text{ mm}^2$ ; MATSUNAMI) on the bottom of the stretch chamber (Figure S1d). After closing the stretch chamber, humid nitrogen gas was passed through the chamber to remove any oxygen from the chamber. After passing the nitrogen gas for 30 min, the stretcher part equipped with the elastomer substrate was lowered until it contacted the ATP buffer on the bottom cover glass to initiate motility of microtubules. The time of ATP addition was set as  $-125 \text{ min}$  before application of stretching, and microscopic observation was initiated. The aforementioned experiments were performed at  $23 \text{ }^\circ\text{C}$ .

**Application of stretching stimuli:** We used a stretch chamber to apply a stretching stimulus to moving microtubules.<sup>36</sup> The stretch chamber was mounted on an inverted light microscope and was connected to a N<sub>2</sub> gas line so that the stretching experiment could be conducted in an inert atmosphere.<sup>47,48</sup> The elastomer substrate attached to the movable frame was elongated to the specified length using a computer-controlled stepping motor (SGSP-13ACT-B0; Sigma-Koki) at the prescribed strain rate, which was then followed by compression back to its initial length. The stretching stimulus was applied to the microtubules in two different manners: single-step and cyclic stretching. In the single-step stretching experiment, the microtubules were subjected to single uniaxial stretching stimulus of different stretch strains ( $\epsilon = 10\%$ , 20%, 30%, 50% and 75%) at a stretch strain rate of 0.012 s<sup>-1</sup> after 2 hours of ATP addition. At a stretch strain of 20%, the stretching stimulus was applied to microtubules at different strain rates (0.012 s<sup>-1</sup>, 0.04 s<sup>-1</sup> and 0.2 s<sup>-1</sup>). In the cyclic stretching experiment, a uniaxial cyclic stretching stimulus was continuously applied to microtubules at the threshold stretching strain,  $\epsilon_c = 20\%$ , at different stretch frequencies (0.03 Hz, 0.1 Hz, 0.5 Hz and 1.0 Hz), except for a short pausing time (2 min) for image acquisition.

**Application of radial stretching:** Radial stretching was applied to microtubules by employing an indentation chamber (Figure 5a-c). To apply radial stretching, we pressed a spherical-shaped indenter chip connected with a stepping motor into the silicone elastomer surface (15 × 15 × 0.05 mm<sup>3</sup>, L × W × T; Fuso Rubber Industry Co., Ltd) fixed to the indentation chamber and then returned it back to the initial position by 10 mm and  $\dot{\epsilon} = 0.08$  mm s<sup>-1</sup>.

**Microscopic image capture:** The samples were illuminated with a 100W mercury lamp and visualised with an epifluorescence microscope (Eclipse Ti, Nikon) using an oil-coupled Plan Apo 60 × 1.40 objective (Nikon) and a dry Plan Fluor 20 × 0.50 objective (Nikon). Filter blocks with UV-cut specifications (TRITC: EX540/25, DM565, BA606/55; GFP-HQ: EX455-485, DM495, BA500-545;

Nikon) were used in the optical path of the microscope to allow for visualisation of samples. Images and movies were captured using a CMOS camera (Neo sCMOS; Andor) connected to a PC. To capture a field of view for more than several minutes, ND filters (ND4, 25% transmittance) were inserted into the illuminating light path of the fluorescence microscope to avoid photobleaching.

**Image analysis for orientation of gliding microtubules:** Movies of the microtubules captured by fluorescence microscopy were analysed using Adobe Photoshop CC and Image J, including “Image J plugin Orientation J” (<http://bigwww.epfl.ch/demo/orientation/>) and “MTrack J” (<http://www.imagescience.org/meijering/software/mtrackj/>). We used Orientation J, which quantifies the anisotropy of microtubules by calculating the pixel intensity of a specified area (2560 × 2160 pixels), to obtain circular histograms of the frequency of the angle between microtubule and the stretch axis.

**Calculation of the nematic order parameter,  $S$ :** The nematic order parameter,  $S$  was calculated by using Equation (1).<sup>20</sup>

$$S = \frac{1}{N_{MT}} \sqrt{\left(\sum_{i=0}^{180} R_i \cos 2\theta_i\right)^2 + \left(\sum_{i=0}^{180} R_i \sin 2\theta_i\right)^2} \quad (1)$$

where  $N_{MT}$  refers to total number of pixels involved to microtubules in a movie frame detected by sliding the Gaussian analysis window applied to the fluorescence intensity distribution over the entire image.  $\theta_i$  is the local angle of a group of microtubules against the stretch axis, which was evaluated for every pixel of the image of microtubules based on the structure tensor. The range of  $\theta_i$  was fixed from 0° to 180° based on the symmetry of horizontally aligned microtubules with respect to the stretching direction.  $R_i$  is the frequency at the angles  $\theta_i$ .  $S = 0$  and  $S = 1$  represents random and oriented alignment of microtubules, respectively.

**Computer simulations:** In this work, we performed two different computer simulations. One is a Brownian dynamics simulation of individual microtubules at low density ( $n = 100$ ) to visualize the morphology of microtubules aligned at different angles during cyclic stretching, which supports our theoretical considerations on the angle of no elongation/compression. Another is a Vicsek model based simulation to elucidate how the nematic interaction between microtubules affects their orientation at high density condition when it is biased by pre-oriented microtubules, which is mimicking the posterior orientation process of microtubules after finishing the application of stretching (Supplementary discussion).

**Brownian dynamics simulation (single microtubule / stretched surface interaction *via* kinesin):**

The method for Brownian dynamics simulations of the individual microtubules was adapted for this study from previous works.<sup>36, 39</sup> Briefly, we simulated the three-dimensional movement of microtubules propelled by kinesin motors on compression of the substrate. The microtubules were subject to the constraint:

$$z \geq 0 \quad (2)$$

We consider the microtubules to be infinitely thin and inextensible semi-flexible bead-rod polymers with a bending stiffness of  $11.0 \text{ pN} \cdot \mu\text{m}^2$ . The length of microtubules was set at  $20 \mu\text{m}$ , corresponding to the most frequent value of the distribution of microtubule length in our experiment, and each simulated microtubule consisted of 40 rigid segments. Microtubule movement was simulated with Brownian dynamics under the constraint of fixed segment length.

Kinesin motors were randomly distributed over the allowed surfaces by specifying the positions of the kinesin tails. The surface density of kinesins was set to  $40 \mu\text{m}^{-2}$ . The contraction of the substrate was simulated by changing positions of kinesin tails  $(x_{tail,i}(t), y_{tail,i}(t))$  with the following expressions:

$$x_{tail,i}(t) = x_{0,tail,i} + \frac{\varepsilon_{max}}{2}(1 - \cos(2\pi ft))x_{0,tail,i} \quad (3)$$

$$y_{tail,i}(t) = y_{0,tail,i} - \frac{\nu\varepsilon_{max}}{2}(1 - \cos(2\pi ft))y_{0,tail,i} \quad (4)$$

where  $\varepsilon_{max}$  is the maximum strain (0.2),  $\sigma$  is the Poisson ratio,  $f$  is the frequency of the stretching (0.1 Hz),  $x_{0,tail,i}$  and  $y_{0,tail,i}$  are the positions of kinesin tails without any strain. According to our measurement, the Poisson ratio was a function of strain ( $\varepsilon$ ) and can be well described as:

$$\sigma(\varepsilon) = 0.5 - 0.45(1 - e^{-1.2\varepsilon}) \quad (5)$$

We set  $\nu$  to 0.45 for the strain of 20% which is used in the experiment. If a microtubule segment came close to a kinesin motor tail within a capture radius ( $w = 20$  nm),<sup>49</sup> the kinesin motor was assumed to be bound to the microtubule segment, and the position of the motor head was specified on the microtubule segment. The bound kinesin acted as a linear spring between the motor head and tail with the spring constant of  $100 \text{ pN } \mu\text{m}^{-1}$  and with zero equilibrium length, and exerted a pulling force on the microtubule segment. The pulling force was divided into two forces which acted on the two beads located at either end of the microtubule segment where the kinesin motor was bound, under the condition that the total force and torque on the segment remained the same.

The head of the bound kinesin motor moved toward the microtubule plus end with a force-dependent velocity expressed as

$$v(F_{\parallel}) = v_0 \left(1 - \frac{F_{\parallel}}{F_{stall}}\right) \quad (6)$$

where  $v_0$  is the translational velocity without applied forces,  $F_{\parallel}$  is the component of the pulling force along the microtubule, and  $F_{stall}$  is the stall force of kinesin motors.  $v_0$  was set at  $0.4 \mu\text{m s}^{-1}$ ;  $F_{stall}$  was set at  $5 \text{ pN}$ .<sup>50</sup>

A kinesin motor bound to a microtubule was assumed to detach either when the pulling force exceeded the detachment force of  $7 \text{ pN}$ ,<sup>40</sup> or when the kinesin reached the microtubule plus end. We neglected spontaneous dissociations of kinesin motors from microtubules. The simulation result was visualized with ParaView (<http://www.paraview.org/>).

## **ACKNOWLEDGMENTS**

We would like to thank Mr. Yasutaka Sasaki for his cooperation in constructing the device to apply stretching to microtubules (stretch chamber). This research was financially supported by a Grant-in-Aid for Scientific Research on Innovative Areas (grant Number JP24104004 and 18H05423) and Grant-in-Aid for Scientific Research (A) (grant number 18H03673). D. I. is supported by Grant-in-Aid for JSPS Fellows (grant number 14J02648). H.H. is supported by NSF-DMR grant 1807514.

## **Author Contributions**

D.I., T.N., A.M.R.K., K.S., A.K. and A.K. (Akira Kakugo) conceived and designed the experiments; D.I. performed the experiments and analysed the experimental results; G. G., A.K. and T.N. performed the simulation; K.T. purified MAP4-fragment; D.I., G. G., T. N., A.M.R.K., H. H. and A.K. (Akira Kakugo) wrote the paper.

**Supporting Information Available:** The supporting information file includes supporting discussion, references, supporting figures. S1 to S19, movie legends for Movies S1 to S8. These materials are available free of charge on the ACS Publications website at <http://pubs.acs.org>.

## REFERENCES

1. Vicsek, T.; Czirók, A.; Ben-Jacob, E.; Cohen, I.; Shochet, O. Novel Type of Phase Transition in a System of Self-Driven Particles. *Phys. Rev. Lett.* **1995**, *75*, 1226–1229.
2. Marchetti, M. C.; Joanny, J. F.; Ramaswamy, S.; Liverpool, T. B.; Prost, J.; Rao, M.; Aditi Simha, R. Hydrodynamics of Soft Active Matter. *Rev. Mod. Phys.* **2013**, *85*, 1143–1189.
3. Grzybowski, B.A.; Fitzner, K.; Paczesny, J.; Granick, S. From Dynamic Self-Assembly to Networked Chemical Systems. *Chem. Soc. Rev.* **2017**, *46*, 5647–5678.
4. Needleman, D.; Dogic, Z. Active Matter at the Interface Between Materials Science and Cell Biology. *Nat. Rev. Mater.* **2017**, *2*, 17048.
5. Kiatkirakajorn, P. C.; Goehring, L. Formation of Shear Bands in Drying Colloidal Dispersions. *Phys. Rev. Lett.* **2015**, *115*, 088302.
6. Reynolds, C. W. Flocks, Herds, and Schools: A Distributed Behavioral Model. *Comp. Graph.* **1987**, *21*, 25–34.
7. Couzin, I. D. Collective Cognition in Animal Groups. *Trends. Cogn. Sci.* **2009**, *13*, 36–43.
8. Kraikivski, P.; Lipowsky, R.; Kierfeld, J. Enhanced Ordering of Interacting Filaments by Molecular Motors. *Phys. Rev. Lett.* **2006**, *96*, 258103.
9. Berdahl, A.; Torney, C. J.; Ioannou, C. C.; Faria, J. J.; Couzin, I. D. Emergent Sensing of Complex Environments by Mobile Animal Groups. *Science* **2013**, *339*, 574–576.
10. Wioland, H.; Woodhouse, F. G.; Dunkel, J.; Goldstein, R. E. Ferromagnetic and Antiferromagnetic Order in Bacterial Vortex Lattices. *Nat. Phys.* **2016**, *12*, 341–345.
11. Palacci, J.; Sacanna, S.; Steinberg, A. P.; Pine, D. J.; Chaikin, P. M. Living Crystals of Light-Activated Colloidal Surfers. *Science* **2013**, *339*, 936–940.
12. Bricard, A.; Caussin, J. B.; Desreumaux, N.; Dauchot, O.; Bartolo, D. Emergent Vortices in Populations of Colloidal Rollers. *Nature* **2013**, *503*, 95–98.
13. Nedelec, F. J.; Surrey, T.; Maggs, A. C.; Leibler, S. Self-Organization of Microtubules and

Motors. *Nature* **1997**, *389*, 305–308.

14. Schaller, V.; Weber, C.; Semmrich, C.; Frey, E.; Bausch, A. R. Polar Patterns of Driven Filaments. *Nature* **2010**, *467*, 73–77.

15. Schaller, V.; Weber, C.; Hammerich, B.; Frey, E.; Bausch, A. R. Frozen Steady States in Active Systems. *Proc. Natl. Acad. Sci. USA* **2011**, *108*, 19183–19188.

16. Luria, I.; Crenshaw, J.; Downs, M. E.; Agarwal, A.; Seshadri, S. B.; Gonzales, J.; Idan, O.; Kamcev, J.; Katira, P.; Pandey, S.; Nitta, T.; Phillpot, S. R.; Hess, H. Microtubule Nanospool Formation by Active Self-Assembly is not Initiated by Thermal Activation. *Soft Matter* **2011**, *7*, 3108–3115.

17. Tamura, Y.; Kawamura, R.; Shikinaka, K.; Kakugo, A.; Osada, Y.; Gong, J. P.; Mayama, H. Dynamic Self-Organization and Polymorphism of Microtubule Assembly through Active Interactions with Kinesin. *Soft Matter* **2011**, *7*, 5654–5659.

18. Sumino, Y.; Nagai, K. H.; Shitaka, Y.; Tanaka, D.; Yoshikawa, K.; Chaté, H.; Oiwa, K. Large-Scale Vortex Lattice Emerging from Collectively Moving Microtubules. *Nature* **2011**, *483*, 448–452.

19. Sanchez, T.; Chen, D. T. N.; DeCamp, S. J.; Heymann, M.; Dogic, Z. Spontaneous Motion in Hierarchically Assembled Active Matter. *Nature* **2012**, *491*, 431–435.

20. Inoue, D.; Mahmot, B.; Kabir, A. M. R.; Farhana, T. I.; Tokuraku, K.; Sada, K.; Konagaya, A.; Kakugo, A. Depletion Force Induced Collective Motion of Microtubules Driven by Kinesin. *Nanoscale* **2015**, *7*, 18054–18061.

21. VanDelinder, V.; Brener, S.; Bachand, G. D. Mechanisms Underlying the Active Self-Assembly of Microtubule Rings and Spools. *Biomacromolecules* **2016**, *17*, 1048–1056.

22. Farhadi, L.; Fermino Do Rosario, C.; Debold, E. P.; Baskaran, A.; Ross, J. L. Active Self-Organization of Actin-Microtubule Composite Self-Propelled Rods. *Front. Phys.* **2018**, *6*, 75.

23. Nicolau Jr., D. V.; Lard, M.; Korten, T.; van Delft, F. C. M. J. M.; Persson, M.; Bengtsson, E.;

- Månsson, A.; Diez, S.; Linke, H.; Nicolau, D. V. Parallel Computation with Molecular-Motor-Propelled Agents in Nanofabricated Networks. *Proc. Natl. Acad. Sci. USA* **2016**, *113*, 2591–2596.
24. Huang, Y. M.; Uppalapati, M.; Hancock, W. O.; Jackson, T. N. Microtubule Transport, Concentration and Alignment in Enclosed Microfluidic Channels. *Biomed Microdevices* **2007**, *9*, 175–184.
25. Schaller, V.; Weber, C.; Frey, E.; Bausch, A. R. Polar Pattern Formation: Hydrodynamic Coupling of Driven Filaments. *Soft Matter* **2011**, *7*, 3213–3218.
26. Guillamat, P.; Ignés-Mullol, J.; Sagués, F. Control of Active Liquid Crystals with a Magnetic Field. *Proc. Natl. Acad. Sci. USA* **2016**, *113*, 5498–5502.
27. Guillamat, P.; Ignés-Mullol, J.; Sagués, F. Taming Active Turbulence with Patterned Soft Interfaces. *Nat. Commun.* **2017**, *8*, 564.
28. Peng, C.; Turiv, T.; Guo, Y.; Wei, Q. H.; Lavrentovich, O. D. Command of Active Matter by Topological Defects and Patterns. *Science* **2016**, *354*, 882–885.
29. Takemasa, T.; Yamaguchi, T.; Yamamoto, Y.; Sugimoto, K.; Yamashita, K. Oblique Alignment of Stress Fibers in Cells Reduces the Mechanical Stress in Cyclically Deforming Fields. *Eur. J. Cell Biol.* **1998** *77*, 91–99.
30. Thorn, C. E.; Welford, M. R. The Equilibrium Concept in Geomorphology. *Ann. Assoc. Am. Geogr.* **1994**, *84*, 666–696.
31. Baum, B.; Georgiou, M. Dynamics of Adherens Junctions in Epithelial Establishment, Maintenance, and Remodelling. *J. Cell Biol.* **2011**, *192*, 907–917.
32. Spellings, M.; Engel, M.; Klotsa, D.; Sabrina, S.; Drews, A. M.; Nguyen, N. H.; Bishop, K. J.; Glotzer, S. C. Shape Control and Compartmentalization in Active Colloidal Cells. *Proc Natl Acad Sci U. S. A.* **2015**, *112*, 4642–4650.
33. Park, J. A.; Atia, L.; Mitchel, J. A.; Fredberg, J. J.; Butler, J. P. Collective Migration and Cell Jamming in Asthma, Cancer and Development. *J. Cell Sci.* **2016**, *129*, 3375–3383.

34. Hamant, O.; Heisler, M. G.; Jönsson, H.; Krupinski, P.; Uyttewaal, M.; Bokov, P.; Corson, F.; Sahlin, P.; Boudaoud, A.; Meyerowitz, E. M.; Couder, Y.; Traas, J. Developmental Patterning by Mechanical Signals in Arabidopsis. *Science* **2008**, *322*, 1650–1655.
35. Keeley, A.; Soldati, D. The Glideosome: A Molecular Machine Powering Motility and Host-Cell Invasion by Apicomplexa. *Trends Cell Biol.* **2004**, *14*, 528–32.
36. Inoue, D.; Nitta, T.; Kabir, A. M. R.; Sada, K.; Gong, J. P.; Konagaya, A.; Kakugo, A. Sensing Surface Mechanical Deformation Using Active Probes Driven by Motor Proteins. *Nat. Commun.* **2016**, *7*, 12557.
37. Clemmens, J.; Hess, H.; Lipscomb, R.; Hanein, Y.; Böhringer, K. F.; Matzke, C. M.; Bachand, G. D.; Bunker, B. C.; Vogel, V. Mechanisms of Microtubule Guiding on Microfabricated Kinesin-Coated Surfaces: Chemical and Topographic Surface Patterns. *Langmuir* **2003**, *19*, 10967–10974.
38. Nitta, T.; Tanahashi, A.; Hirano, M.; Hess, H. Simulating Molecular Shuttle Movements: Towards Computer-Aided Design of Nanoscale Transport Systems. *Lab Chip* **2006**, *6*, 881–885.
39. Ishigure, Y.; Nitta, T. Understanding the Guiding of Kinesin/Microtubule-Based Microtransporters in Microfabricated Tracks. *Langmuir* **2014**, *30*, 12089–12096.
40. Kawaguchi, K.; Ishiwata, S. Nucleotide-Dependent Single- to Double-Headed Binding of Kinesin. *Science* **2001**, *291*, 667–669.
41. Mitchell, N. P.; Koning, V.; Vitelli, V.; Irvine, W. T. M. Fracture in Sheets Draped on Curved Surfaces. *Nat. Mater.* **2017**, *16*, 89–93.
42. Vitelli, V.; Lucks, J. B.; Nelson, D. R. Crystallography on Curved Surfaces. *Proc. Natl. Acad. Sci. USA* **2006**, *103*, 12323–12328.
43. Castoldi, M.; Popov, A. V. Purification of Brain Tubulin Through Two Cycles of Polymerization-Depolymerization in a High-Molarity Buffer. *Protein Express. Purif.* **2003**, *32*, 83–88.
44. Case, R. B.; Pierce, D. W.; Nora, H. B.; Cynthia, L. H.; Vale, R. D. The Directional Preference

- of Kinesin Motors is Specified by an Element outside of the Motor Catalytic Domain. *Cell* **1997**, *90*, 959–966.
45. Tokuraku, K.; Noguchi, T. Q. P.; Nishie, M.; Matsushima, K.; Kotani, S. An Isoform of Microtubule-Associated Protein 4 Inhibits Kinesin-Driven Microtubule Gliding. *J. Biochem.* **2007**, *141*, 585–591.
46. Peloquin, J.; Komarova, Y.; Borisy, G. Conjugation of Fluorophores to Tubulin. *Nat. Methods.* **2005**, *2*, 299–303.
47. Kabir, A. M. R.; Inoue, D.; Hamano, Y.; Mayama, H.; Sada, K.; Kakugo, A. Biomolecular Motor Modulates Mechanical Property of Microtubule. *Biomacromolecules* **2014**, *155*, 1797–1805.
48. Kabir, A. M. R.; Inoue, D.; Afrin, T.; Mayama, H.; Sada, K.; Kakugo, A. Buckling of Microtubules on a 2D Elastic Medium. *Sci. Rep.* **2015**, *5*, 17222.
49. Liu, T. W. Flexible Polymer Chain Dynamics and Rheological Properties in Steady Flows. *J. Chem. Phys.* **1989**, *90*, 5826–5842.
50. Howard, J. *Mechanics of Motor Proteins and the Cytoskeleton*; Sinauer Associates: Sunderland, 2001; pp252–255.

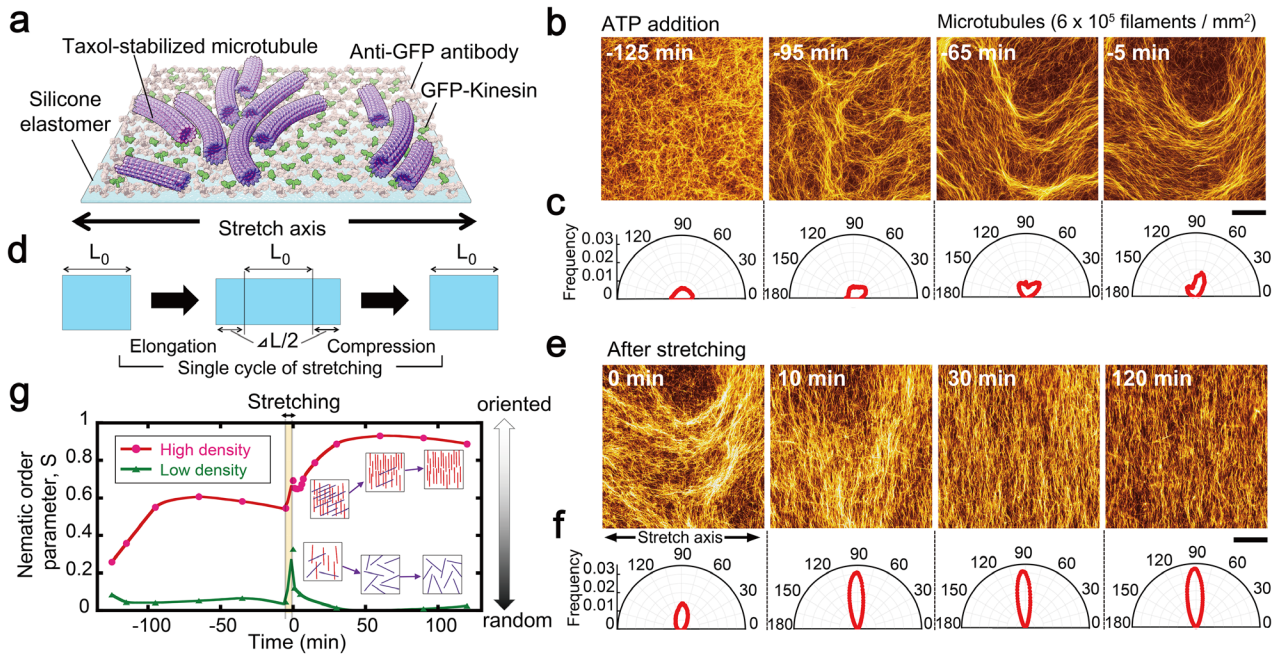


**Figure 1.** Preferential alignment of microtubules under uniaxial single-step stretching stimulus. (a) Schematic diagram showing the *in vitro* gliding assay of microtubules on an elastomer substrate (b, e). Time evolution of streaming flow formation of microtubules before and after the application of uniaxial stretching of 75% final strain at a stretching rate of  $0.012 \text{ s}^{-1}$ . The time of application of stretching was set as 0 min. The length and mean velocity of microtubules were  $20.0 \pm 10.0 \text{ }\mu\text{m}$  and  $180 \pm 20 \text{ nm s}^{-1}$  (mean  $\pm$  s.d.), respectively. Scale bars:  $50 \text{ }\mu\text{m}$ . (c, f) Circular histograms showing the distribution of the orientation angles of microtubules,  $\theta$  ( $0^\circ \leq \theta \leq 180^\circ$ ) before and after the application of the stretching. (d) Definition of stretching strain;  $\varepsilon = \frac{\Delta L}{L_0} \times 100$  (%) where  $L_0$  is initial length of substrate ( $6.8 \text{ mm}$ ) and  $\Delta L$  is the change of length ( $\text{mm}$ ) after applying strain. (g) Time course of the nematic order parameter,  $S$  at the high-density condition ( $\rho = \sim 6 \times 10^5$  filaments per  $\text{mm}^2$ ) of microtubules where streaming flow was observed and at the low-density condition ( $\rho = \sim 5 \times 10^4$  filaments per  $\text{mm}^2$ ) when streaming flow is absent. The stretching strain and strain rate were 75% and  $0.012 \text{ s}^{-1}$ .

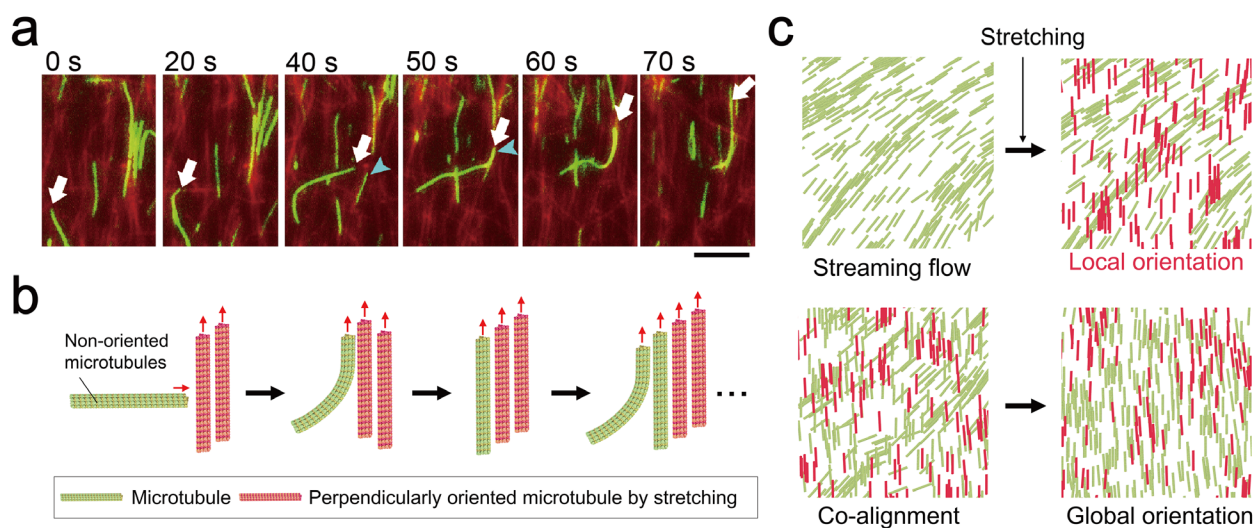


**Figure 2.** Amplification of the preferential alignment of microtubules by nematic interaction between microtubules. (a) Derailment of an individual microtubule from the global orientation of the flow after a horizontal stretching stimulus. Time-lapse fluorescence microscopy images show the movement of a single microtubule (a green microtubule pointed at with a white arrow) while derailing from the global perpendicular orientation of the microtubules. The microtubule moves initially upward (0 s), and is beginning to move right after encountering another microtubule (20 s). However, the rightward movement (40 s) is quickly arrested by another interaction (50 s) and upward movement is restored (60 s, 70 s). Here, TAMRA and Alexa488-labelled microtubules were mixed at a molar ratio of 7.3:1 to visualize the behaviour of individual microtubules in a perpendicular alignment of microtubules. Scale bar: 10  $\mu\text{m}$ . (b, c) Schematic drawing to show amplification of microtubule orientation after stopping the application of stretching. b is showing a local alignment by nematic interaction between microtubules. c is a transition from the streaming flow to the perpendicularly oriented flow *via* nematic interaction.

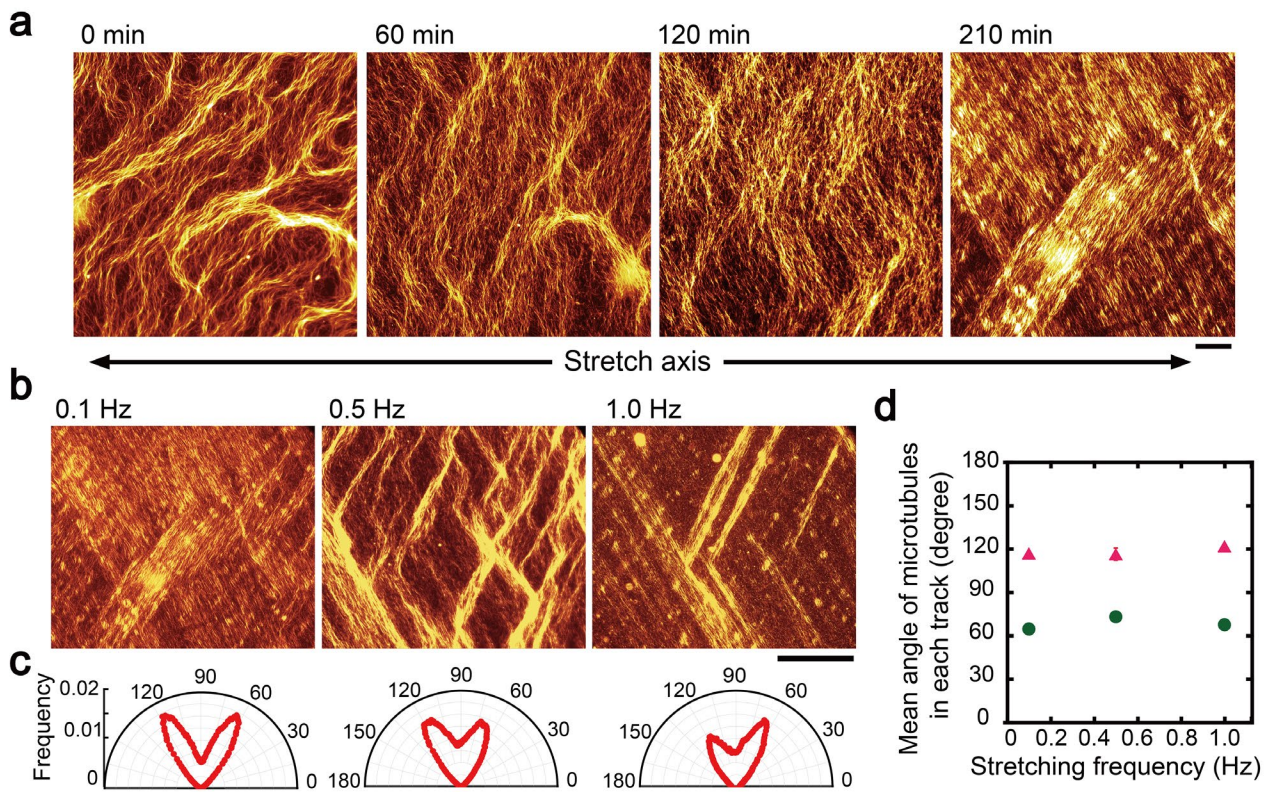


**Figure 3.** Zigzag pattern formation of microtubules under cyclic stretching stimuli. (a) Fluorescence microscopy images showing the time course of the reorganization of a streaming flow of microtubules under uniaxial cyclic stretching stimuli at the threshold stretching strain,  $\varepsilon = 20\%$  and the stretching frequency of 0.1 Hz. Scale bar: 50  $\mu\text{m}$ . (b) Zigzag patterns of microtubules observed at different stretch frequencies of 0.1 Hz, 0.5 Hz and 1.0 Hz, at a fixed stretching strain of  $\varepsilon_c = 20\%$ . Scale bar: 200  $\mu\text{m}$ . Those representative images were captured after 210 min, 60 min and 120 min of application of stretching when a steady state has been reached. (c) Circular histograms showing the distribution of microtubules orientation angles before stretching and at different stretching frequencies of 0.1, 0.5 and 1.0 Hz. (d) Mean orientation angles of gliding microtubules in zigzag patterns at different stretching frequencies. The orientation angles were measured after 120 min of cyclic stretching with 20% strain.

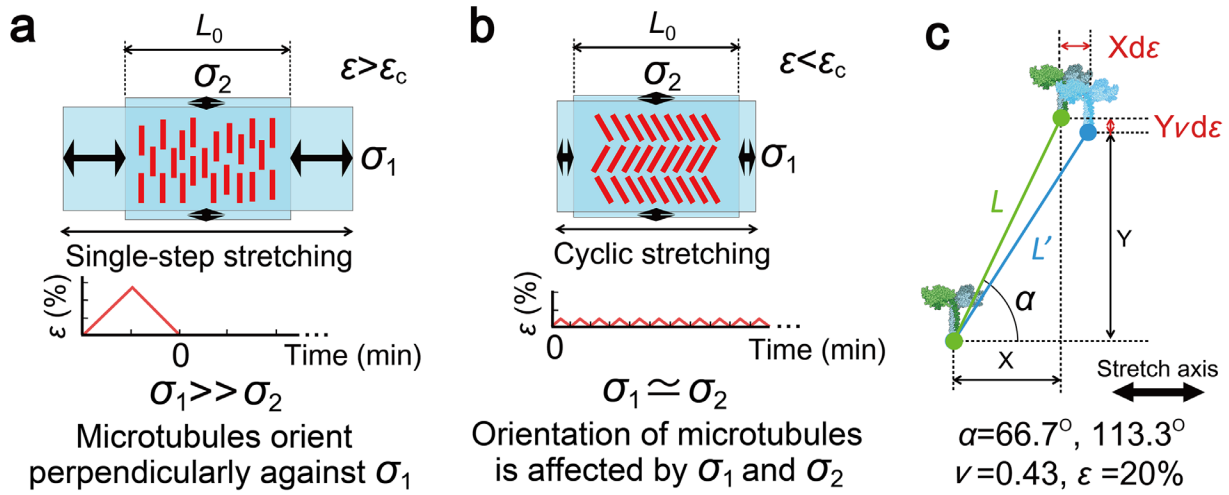


**Figure 4.** Theoretical models of microtubule orientation under stretching. (a, b) Schematic diagram of the deformation of elastomer substrate during a single-step stretching ( $\varepsilon > \varepsilon_c$ ) and cyclic stretching ( $\varepsilon < \varepsilon_c$ ). The graphs indicate the methods to apply stretching. Red bars on the substrate indicate microtubules forming perpendicular orientation against stretching axis and zigzag pattern. The  $\sigma_1$  and  $\sigma_2$  are the first (maximum) and second principal stress, respectively. (c) Geometrical model to attain characteristic orientation angles during cyclic stretching. The schematic diagram is showing coordinate movement of kinesin after elongation of the substrate.  $L$  and  $L'$  indicate the distance between two kinesins before and after elongation of the substrate.  $\alpha$  is the angle between the horizontal line and the line connecting two kinesins before elongation of the substrate.  $\text{Arctan}(1/\nu)$  at Poisson ratio,  $\nu = 0.43$  and  $\varepsilon = 20\%$  gives the characteristic angles  $66.7^\circ$  and  $113.3^\circ$  at which the  $L'$  becomes equal to the  $L$ .

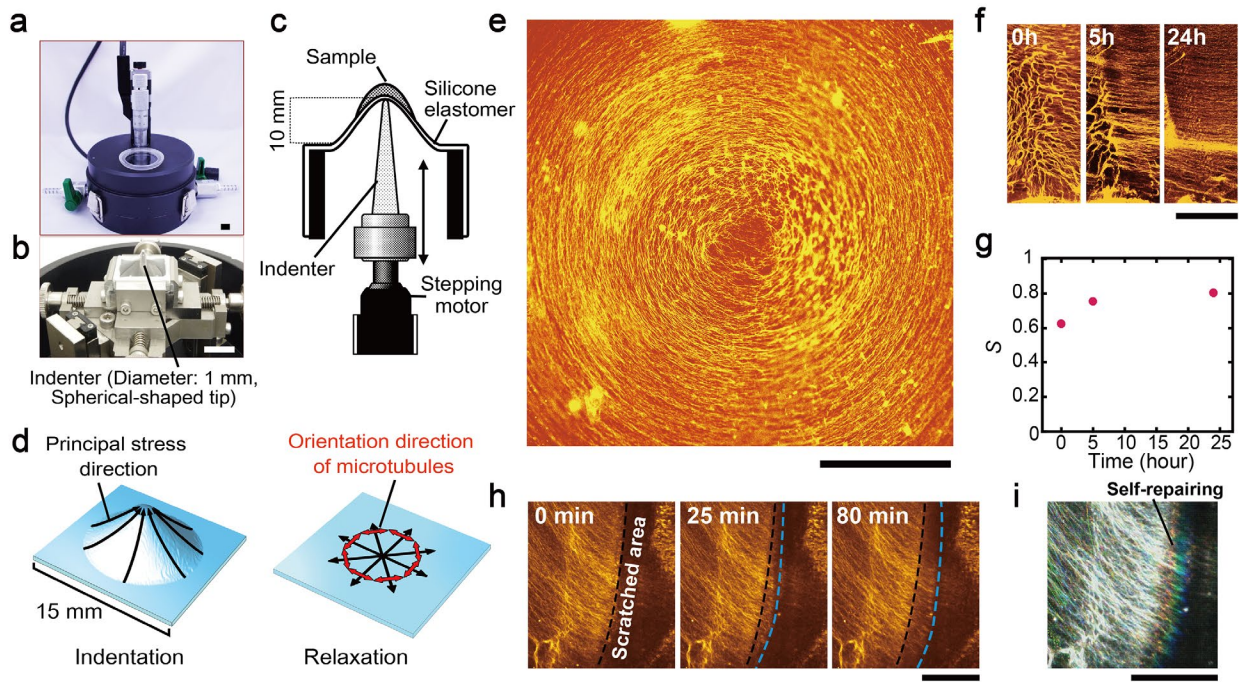


**Figure 5.** Emergence of a large vortex under radial strain at the substrate. Experimental setup used to indent the silicone substrate where gliding microtubules are forming streaming flow. Outer (a) and inner (b) view of the indentation chamber. Scale bars: 1 cm. (c) A schematic diagram showing the indenter part of the indentation chamber and (d) Orientation of microtubules predicted from the stretch direction after application of radial stretching. (e) Fluorescence microscopy image showing the formation of a large vortex from microtubules under radial stretching with the indentation depth of 10 mm at  $\dot{\epsilon} = 0.08 \text{ mm s}^{-1}$ . Scale bar: 1 mm. (f) Spatiotemporal orientation of microtubules at the periphery of vortex. Scale bar: 1 mm. (g) Time dependent change of the order parameter in Figure 5f. (h) Time lapse fluorescence microscopy images showing the self-repair of the damaged part (scratched) of vortex of microtubules. Initially the boundary between the scratched and intact part of the vortex is marked by the black broken line which moves over time as the repair progresses (blue broken line). Scale bar: 250  $\mu\text{m}$ . (i) Time overlaid image of Figure 5h. Scale bar: 250  $\mu\text{m}$ .